On the spiking stages in deep transition and unsteady separation

ROBERT I. BOWLES[1], CHRISTOPHER DAVIES[2] and FRANK T. SMITH[1]

[1]*Department of Mathematics, University College London, Gower Street, London WC1E6BT, UK*
[2]*School of Mathematics, Cardiff University, P.O. Box 926, Cardiff, CF24 4YH, UK*

Abstract. Numerical simulations of a large-amplitude nonlinear two-dimensional train of Tollmien-Schlichting waves are performed first and show the development of short-scaled structures or spikes. A careful description of the spiking process and its subsequent development is given describing the generation of localized maxima in the streamwise pressure distribution and associated vortices, spikes in a perturbation velocity trace and the emergence of strong wall-normal pressure gradients. A high-Reynolds-number asymptotic theory has previously been developed by two of the authors which aims to describe this spiking process. The current work is the first to give a comparison between this theory and planar Navier-Stokes computations. We give a brief description of the theory showing how normal pressure gradients become active and their role in the generation of the streamwise pressure distribution and its subsequent effects such as vortex generation and wall-layer vorticity eruptions. The presentation is given with close qualitative reference to the simulations, so giving credence to the relevance of the theoretical account and an interpretation of that account in physical terms. The comparison, although primarily qualitative, is successful in that it is possible to identify the physical processes highlighted by the theory in the computations, so clarifying the complex fluid motions and suggesting directions for further research. The paper concludes with firstly a discussion of how the results of the simulations and the theory could be used to give an understanding of similar processes seen in unsteady planar separation and secondly their relevance to the strongly three-dimensional processes at work in deep transition experiments.

Key words: boundary-layer transition, breakdown, separation, spikes, vortices

1. Introduction

The formation of 'spikes', short-scaled and large-amplitude events in a trace of disturbance velocity against time, is a fairly universal phenomenon in transition of wall-bounded shear flows to turbulence at medium-to-high Reynolds numbers. They herald the start of 'late' or 'deep' transition, where linear or weakly nonlinear descriptions of the flow fail. They have been seen in experimental and computational studies of boundary-layer transition, both in the K and N-type routes, and in channel and pipe flows [1–4].

Careful experiments and direct numerical simulations of the transition process have shown several physical phenomena are associated with the spikes [5,2]. Firstly they have a streamwise length-scale significantly shorter than the wave upon which they ride and they often occur at the head of a downstream-pointing Λ-shaped vortex structure. Secondly, between the legs of this Λ vortex the spanwise vorticity is concentrated in a local high shear layer which separates the slower moving flow, brought up from near the wall by the circulation about the legs, from the faster flow further from the wall. At the head of the vortex this shear layer and the vorticity in the legs are seen to merge. Thirdly this vorticity is observed to roll up to form vortices with regions of recirculating flow when viewed in a frame traveling with the disturbance. Associated with each vortex is a localized pressure minimum and regions

where the wall-normal velocity changes in sign. Such vortex generation is also seen in dynamic stall and unsteady separation [6]. Fourthly, these intense vortices develop into strongly three-dimensional Omega-(Ω)shaped vortices which travel downstream relative to the wave, retaining their structure. Interaction between these vortices and with the wall soon leads to breakdown to turbulence.

A theoretical approach that has managed to describe a spiking process and reproduce some of the phenomena listed above is that developed in [7–12]. Its success is in terms of the theory's self-consistency, its providing of physical insight, *e.g.* through scales, and its broad agreement with direct numerical simulations and experiments on three-dimensional flows. The last aspect is particularly important; for instance see the comparisons in [8] with [13]'s experiments concerning the appearance of the first spike. The theoretical approach above considers the flow along the centreline of the Λ-vortex, the peak plane. Indeed, while the real flows in deep transition are certainly three-dimensional and possibly include such three-dimensional phenomena as the Crowe mechanism for vortex line instability, some of the main events would seem to be locally two-dimensional. In that spirit, the current paper first presents a numerical solution of a large-amplitude two-dimensional wavetrain of nonlinear Tollmien-Schlichting (TS) waves in a parallelized boundary layer and second interprets the results in terms of the theoretical description. The aim is thus to combine practical asymptotics with careful numerical simulation and to compare the two. This comparison is predominantly qualitative but is successful in identifying the physical processes predicted to be active at asymptotically large Reynolds number in the finite-Reynolds-number computations. In turn new directions for theoretical research are suggested. The novel contribution here includes this comparison as well as recent theoretical and numerical developments.

From the theoretical viewpoint there are strong similarities between the development of the two-dimensional nonlinear wave flow studied here and the process of unsteady planar boundary-layer separation. Indeed, the flow structures that are seen in our current simulations are very similar to those observed in the computations of vortex-driven separation carried out by [14, 15]. The TS waves generated provoke large regions of separated flow and to some extent the wave train can be viewed as a string of travelling vortices moving downstream within a boundary layer. This point is discussed further in Section 5.

2. Numerical methods

Reference [18] derives a new velocity-vorticity formulation of the Navier-Stokes equations that can be applied in highly efficient numerical simulations of three-dimensional boundary-layer disturbance evolution and control. The numerical results described in the present paper were obtained using a code based upon a two-dimensional version of the new velocity-vorticity formulation. We restrict ourselves here to providing only a very brief account of the governing equations and their numerical discretization. Further details can be found elsewhere, for a variety of applications that involve compliant surfaces, interactive MEMS devices, mean-flow non-parallelism, absolute instability and nonlinear waves [16–26].

2.1. Governing equations

We take as our governing equations the two-dimensional Navier-Stokes equations for $\vec{U} = (U, V)$ with U and V, respectively, the streamwise and wall-normal velocity components and P the pressure.

$$\vec{U}_t + \vec{U} \cdot \nabla \vec{U} = -\nabla P + \nabla^2 \vec{U}/R, \tag{1}$$

$$\nabla \cdot \vec{U} = 0. \tag{2}$$

In this formulation the streamwise and wall-normal distances x and y have been nondimensionalized using the boundary-layer displacement thickness δ, the velocities using the free-stream velocity U_∞ and the time t with the ratio δ/U_∞. The Reynolds number is $R = \delta U_\infty/\nu$, where ν is the kinematic viscosity of the fluid. The boundary conditions are $\vec{U} = 0$ on the wall $y = 0$ and $\vec{U} \to (1, 0)$ as $y \to \infty$.

If we let u, v denote streamwise and wall-normal velocity components corresponding to a two-dimensional deviation from a parallel Blasius flow $\vec{U} = (U_b(y), 0)$, and let ω denote the associated vorticity perturbation, then (1)–(2) can be cast in the form

$$\frac{\partial \omega}{\partial t} + U_b \frac{\partial \omega}{\partial x} + \frac{\partial(u\omega)}{\partial x} + \frac{\partial(v\omega)}{\partial y} + vU_b'' = \frac{1}{R}\nabla^2\omega + \frac{1}{R}U_b''' , \tag{3}$$

$$\nabla^2 v = -\frac{\partial \omega}{\partial x} , \tag{4}$$

$$u = -\int_y^\infty \left(\omega + \frac{\partial v}{\partial x}\right) \mathrm{d}y . \tag{5}$$

It may be noted that the streamwise perturbation velocity component u is defined explicitly in terms of the wall-normal component v and the vorticity perturbation ω. Thus u may be eliminated from the vorticity transport equation, leaving a system of two partial differential equations for the two unknowns ω, v. For the parallelized simulations described herein, we omitted the final term $1/R\, U_b'''$ from the right-hand side of the transport equation. This term would otherwise act as a source for the generation of a non-parallel base flow. There would be no numerical difficulties if the non-parallel source term was retained, as was done in some related, lower amplitude, simulations conducted by [25, 26], using essentially the same technique as we used for the present simulations. We have chosen here to consider a parallel base flow only for the purposes of simplicity, specifically to avoid complications in the comparison of the short-scaled shock structure with the theoretical predictions which might arise due the spatial variation in stability properties of the base flow.

Disturbances are generated using a localized suction/blowing strip centred at a computationally convenient streamwise location $x = x_s$ on the wall surface $y = 0$. Thus we impose the condition $v(x, 0, t) = \bar{v}(x - x_s, t)$, for some localized time-periodic wall-normal velocity distribution $\bar{v}$, which is switched on in a smooth fashion at $t = 0$. We take $\bar{v}(-x, t) = -\bar{v}(x, t)$, to ensure that there is no net mass influx, and $\bar{v}(x, t) = 0$ for $|x| > l$, where the half-width l of the suction/blowing slot is chosen to be shorter, but comparable to, the wavelength of the TS disturbance wave that is to be generated. The no-slip condition $u(x, 0, t) = 0$ is imposed at all streamwise locations. Using the definition of u given above in Equation (5), we can translate this condition into a fully-equivalent integral constraint on the vorticity

$$\int_0^\infty \omega \, \mathrm{d}y = -\int_0^\infty \frac{\partial v}{\partial x} \, \mathrm{d}y . \tag{6}$$

The above integral constraint can then be applied in the discretized version of the vorticity transport equation to provide a direct link between the evolution of the vorticity and the no-slip condition. We thus avoid any form of artificial wall-vorticity boundary condition.

At the inflow boundary $x = x_{in}$ of the computational domain, the null perturbation conditions $v = \omega = 0$ are imposed, whilst at the outflow $x = x_{out}$ we use wavelike conditions which allow small-amplitude disturbances to convect out of the domain without any spurious reflection. In practice, because we considered only two-dimensional disturbances, it was possible to conduct our simulations using a computational domain of sufficient streamwise extent to ensure that the disturbance amplitude remained negligible at the outflow for the evolution times of interest. In other words, the physical behaviour that we were interested in studying could be observed well before any significant disturbance reached the vicinity of the outflow.

2.2. NUMERICAL DISCRETIZATION

Our numerical discretization scheme is essentially a two-dimensional, nonlinear, version of a three-dimensional, linearized, discretization scheme described more fully in [18]. The main features of the numerical scheme that we adopted are as follows: (i) The streamwise variation is discretized using fourth-order accurate compact finite-differences. (ii) Spectral Chebyshev expansions are used for the discretization in the wall-normal direction. A co-ordinate transformation is employed to map the semi-infinite physical domain onto a finite computational domain. (iii) The temporal discretization of the vorticity transport equation is implicit for the viscous term that involves a wall-normal second derivative, but is explicit for all other terms. The integral constraint on the vorticity, which is used to impose the no-slip condition, is also treated in an explicit fashion. (iv) The wall-normal discretization is formulated so as to involve only pentadiagonal matrix operations. This facilitates the direct solution of the discretized vorticity transport equation using a highly efficient Thomas algorithm. The Poisson equation is also solved using a direct method, by combining the Thomas algorithm with a fast sine-transform along the streamwise direction. (See, for example, [27] for an account of a similar direct solution method.) (v) A pseudo-spectral transform technique is used to compute the nonlinear and other product terms that appear in the vorticity transport equation.

We implemented a high-order compact filtering scheme along the streamwise direction, to remove unphysical oscillations at the grid-scale. It was found that, for simulations involving strongly nonlinear disturbances, low-amplitude streamwise grid-scale oscillations could persist when an unfiltered scheme was utilised with a computationally feasible time-step. Checks were made to verify that the results obtained from simulations conducted with and without filtering differed only with respect to the level of numerical noise at the streamwise grid-scale. Grid-refinement studies were also undertaken to provide evidence that the grid-scale oscillations were purely numerical in origin. The filtering scheme that we adopted is similar to schemes that have been employed, successfully, in direct numerical simulations by other investigators. (A careful discussion of the origin and removal of grid-scale oscillations can be found in reference [27], which also contains a more extensive listing of earlier studies.)

The two-dimensional numerical simulation code developed using the discretization scheme outlined above has been extensively tested and validated. (See the references listed at the beginning of this section.) References [25, 26] present details of code validation for the cases of linear and comparatively low amplitude nonlinear disturbance evolution in a Blasius boundary layer that are particularly pertinent to our present investigations.
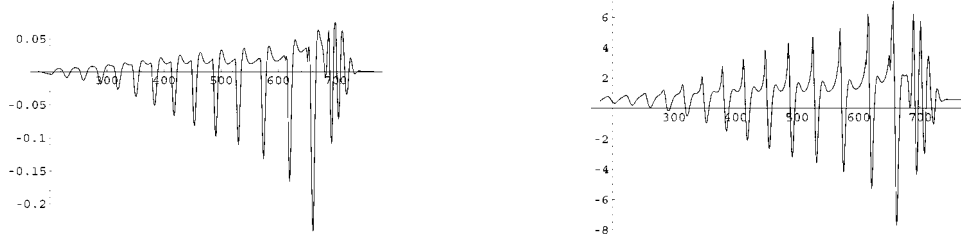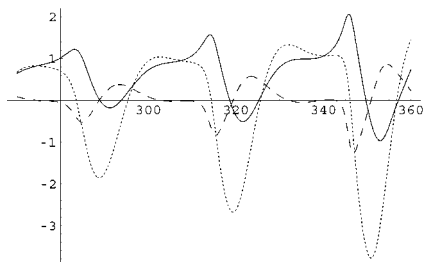
(a) Wall pressure, $P(x, 0)$.

(b) Wall Vorticity $\Omega(x, 0)$.

Figure 1. The wavetrain of TS waves at $R = 2500$. The forcing is centred about $x = 160$.
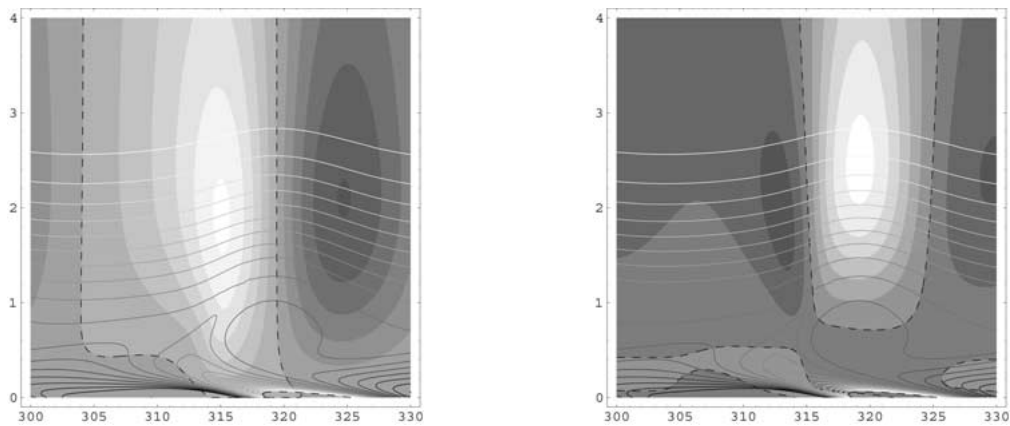
(a) Total vorticity $\Omega(x, y)$ and vertical velocity v. Values of Ω are given by the contours in the range 0·05 (white) to 0·8 (black) in steps of 0·05 with the additional zero contour dashed. Values of v are represented by the shading separated by contours with values $-0·25$ (darkest) to 0·25 (lightest) in steps of 0·05. Again the zero contour is dashed.

(b) Total vorticity $\Omega(x, y)$ and normal pressure gradient $P_y(x, y)$. Ω is given as in Figure 2(a) whilst P_y is represented by the shading separated by contours with values $-0·002$ (darkest) to 0·005 (lightest) in steps of 0·001. The zero line is dashed.

(c) Wall vorticity (solid), wall pressure $500P(x, 0)$ (dotted) and pressure gradient $500P_x(x, 0)$ (dashed) over three periods.

*Figure 2.* The early development of the spike around $x = 315$ at $R = 2500$.

3. Simulation results

The lowest Reynolds number, based on the boundary-layer displacement thickness, for which we present results is $R = 2500$. A wavetrain of nonlinear TS waves is generated by the forcing at $x = x_s = 160$ as is indicated by the wall-pressure, $P(x, 0)$, and total vorticity, $\Omega(x, 0)$, values in Figures 1(a) and 1(b). Here $\Omega = U_b' + \omega$. The amplitude of these waves is large as is indicated by the occurrence of flow separation ($\Omega(x, 0) < 0$) which is first visible at $x = 290$. The waves also exhibit the nonlinear features of relatively short pressure minimum separated by longer-scaled maximum as seen in the computations of [25] and broadly consistent with the asymptotic theory of [28]. We see the first indications of a short-scaled event, which is not explained by this theory, occurring in the wall vorticity trace in the increasingly large positive spike just upstream of the regions of separated flow downstream from $x = 280$. We note that this occurs at a position where the local pressure gradient is favourable. Further downstream at $x = 570, 615, 655$ we see the development of finer structure within these events. We now turn to the details of the flow features in the vicinity of these events, which we shall refer to as 'spikes', during the early stages of their development. Figure 2(a) shows the total vorticity and the vertical velocity over approximately a wavelength around $x = 315$. The boundary-layer edge is at approximately $y = 3$ so that the figures show structures that develop relatively close to the wall near $y = 0.5$. The large wave-amplitudes force separated flow in regions of adverse pressure gradient. These act as sources of decreased vorticity through the equation

$$P_x|_{y=0} = R^{-1}\Omega_y|_{y=0}, \tag{7}$$

which may be derived from (1). In a frame traveling downstream with the wave, the wall moves upstream carrying this vorticity upstream away from its site of generation. As the flow develops, these reduced values are forced rapidly upwards in a primary eruption caused by an region of increased positive vertical velocity which develops relatively close to the wall just upstream of the separation. This is visible at $x = 315$, $y = 0.5$ and is also associated with a locally increasing favourable pressure gradient in its vicinity and the generation of increased values of vorticity in a region even closer to the wall situated just below the maximum in vertical velocity and visible in Figure 2(a) around $x = 314$. The increase can also be seen in Figure 2(c) which shows the shortening of the scale of the structure in addition to the increasing amplitude and the associated increases in the pressure gradient and hence through (7) the wall vorticity. Figure 2(b) shows shaded contours of the wall-normal pressure gradient P_y together with the same contour lines of vorticity as in Figure 2(a) for reference.

The later development of the structure is seen in Figure 3. The figure is in fact taken from a different calculation performed with greater resolution and a larger amplitude forcing but the structures obtained here are typical of those seen around $x = 600$ in Figure 1. The separation region extends from $x = 447$ to 454 approximately and the separation or primary vortex, visible in Figure 3(a) has a width comparable with the boundary-layer thickness. On the upstream side of this we see a secondary vortex in the process of formation, viewed in close up in Figures 3(c)-(e). Associated with that new vortex is a new region of downward velocity at $x = 442$, $y = 0.75$ splitting the original region of upward flow. Although having its origins in two-dimensional dynamics, this process resembles closely the splitting of the shear layer seen in the three-dimensional computations of boundary-layer transition by [5] as the Ω-shaped vortices begin to develop. The downward velocity advects the reduced values of vorticity towards the wall before it is carried upwards once more around the vortex that is so generated and which contains higher values of vorticity (Figure 3(a)). This originated
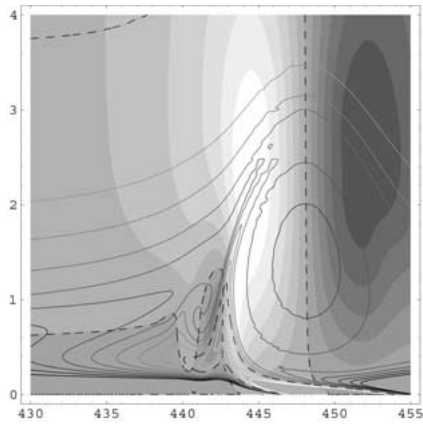
(a) Total vorticity $\Omega(x, y)$ and vertical velocity v. Values of Ω are given by the contours in the range -0.4 (white) to 0.8 (black) in steps of 0.1 with the additional zero contour dashed. Values of v are represented by the shading separated by contours with values -0.1 (darkest) to 0.1 (lightest) in steps of 0.02. Again the zero contour is dashed.
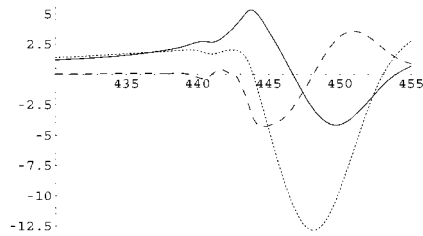

(b) Wall vorticity (solid), wall pressure $100P(x, 0)$ (dotted) and pressure gradient $100P_x(x, 0)$ (dashed).
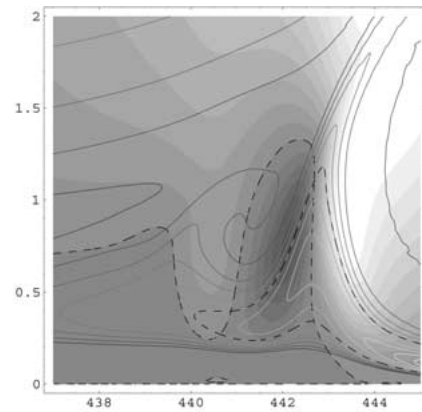
(c) Total vorticity Ω, represented as in Figure 3(a) and v represented by the shading separated by contours with values -0.05 (darkest) to 0.1 (lightest) in steps of 0.01. The zero lines are dashed.
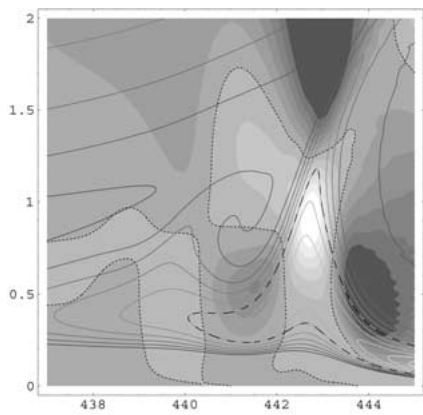
(d) Total vorticity Ω, represented as in Figure 3(a) and normal pressure gradient P_y represented by the shading separated by contours with values -0.01 (darkest) to 0.01 (lightest) in steps of 0.002. The zero lines are dashed.
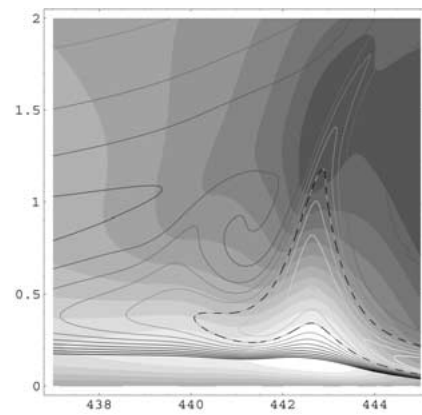
(e) Total vorticity Ω, represented as in Figure 3(a) and perturbation streamwise velocity u represented by the shading separated by contours with values -0.2 (darkest) to 0.2 (lightest) in steps of 0.04.

Figure 3. The subsequent development of the spike at $R = 2500$. Figures 3(c–e) show the structures in Figure 3(a) in more detail.

away from the wall and has now been encircled by vorticity which came from closer to the wall and further downstream. The region of new downward velocity and the vortex position is correlated with the localized pressure maximum that appears at $x = 442$ (Figure 3(b)).

Figure 3(d) shows the normal pressure gradient P_y at this stage. Its value has grown to be comparable with the streamwise gradient. The triangular pattern with vertices at $x = 441 \cdot 5$, $y = 0 \cdot 5$ and $x = 444$, $y = 0 \cdot 5$ (minima) and $x = 442 \cdot 5$, $y = 0 \cdot 8$ (maximum) is typical at this stage. The decay away from the wall of these increased values of P_y occurs between $y = 1$ and $1 \cdot 7$ approximately. The minimum extending above $y = 2$ at $x = 443$ merges with the minimum equivalent to that at $x = 313$ in Figure 2(b) and may be identified with the basic wave. It and its neighbouring maximum are caused by the streamline curvature which may be identified in the behaviour of the vorticity contours across the bulk of the boundary-layer in Figure 2(b). Similar effects, repeated on smaller scales, are responsible for the triangular pattern, which is also seen in 2(b). The zero contour passes through the centre of the secondary vortex so indicating a pressure minimum there. Reference [1] used the development of pressure minimum as characteristics of vortex formation in their computational study of transition in a channel flow.

The perturbation streamwise velocity u is illustrated in Figure 3(e) and shows the negative values that occur at $x = 443$, $y = 1 \cdot 5$ upstream of the expected negative values to be found in the separation vortex just downstream of this figure. These would show up as negative spikes in a trace of perturbation velocity against time and their origin is clearly caused by the reduced vorticity brought up from the wall. In contrast the similar spikes seen in experimental and computational studies of the three dimensional transition process are generally understood to be associated with the reduced streamwise velocities found in the centre of the Ω-shaped vortices. There are regions of increased values close to the wall at $y = 0 \cdot 25$ which are generated by the positive values of vorticity generated there as described above.

We also ran simulations at $R = 10^4$ and $R = 10^5$ and if the Reynolds number is high enough the process of secondary vortex generation caused by the generation of pressure maximum/minimum pairs is repeated. The results illustrated in Figure 4 are from a simulation with similar forcing to that described above but with $R = 10^5$. At these Reynolds numbers the flow development is so rapid that a recognisable wavetrain does not have time to develop and we are then concerned with a form of by-pass transition and a large-amplitude wavepacket. In this packet there is a single large separation region with the two smaller vortices on its upstream side seen clearly in Figure 4(a). A study of the wall pressure in the vicinity of these vortices (Figure 4(b)) shows a series of pressure maxima in the range $x = 294$ to 299. We will consider the complicated behaviour seen around $x = 298 \cdot 5$ below. The wall vorticity values also contain maxima reflecting the pressure distribution. Figures 4(c–e) show that this repetition in the streamwise pressure gradient leads to a corresponding repetition in the structures present in Figure 3 in the plots of v, P_y and u. We would expect to see a second negative spike in a time trace of u for example. We can also see at $x = 294 \cdot 5$, $y = 0 \cdot 6$ the first stages in the generation of a third region of downwards velocity indicating the initial stages of development of a third secondary vortex. Indeed in similar simulations with coarser resolutions such a third vortex was generated. We emphasise that we believe the data shown in Figure 4 to be grid independent. Presumably a further separation is possible at still higher Reynolds numbers or larger amplitudes due to the large adverse pressure gradients that are generated.

At a Reynolds number of 2500 these additional vortices are not seen. Figure 5 illustrates the next stage of development at these lower values by considering an x-station further down-
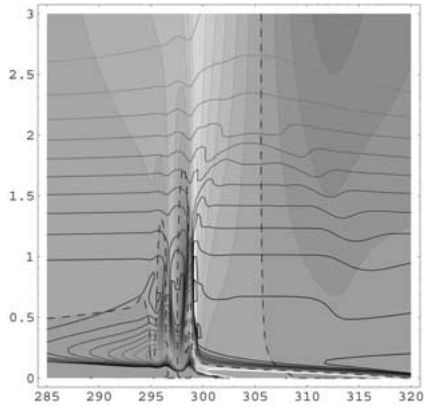
(a) Total vorticity $\Omega(x, y)$ and vertical velocity v. Values of Ω are given by the contours in the range -0.4 (white) to 0.6 (black) in steps of 0.05 with the zero contour dashed. Values of v are represented by the shading separated by contours with values -0.04 (darkest) to 0.04 (lightest) in steps of 0.005. Again the zero contour is dashed.
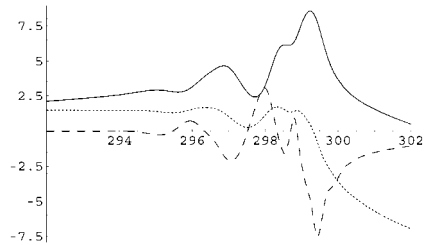

(b) Wall vorticity (solid), wall pressure $300P(x, 0)$ (dotted) and pressure gradient $300P_x(x, 0)$ (dashed).
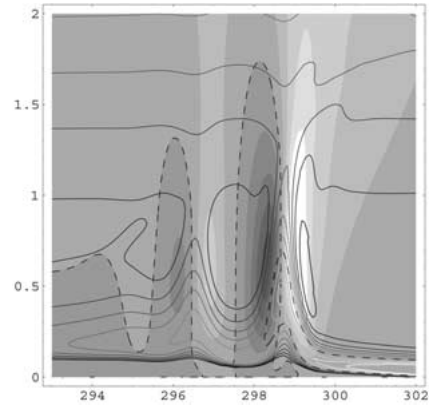
(c) Total vorticity Ω, represented as in Figure 4(a) and normal velocity v represented by the shading separated by contours with values -0.04 (darkest) to 0.04 (lightest) in steps of 0.01. The zero contours are dashed.
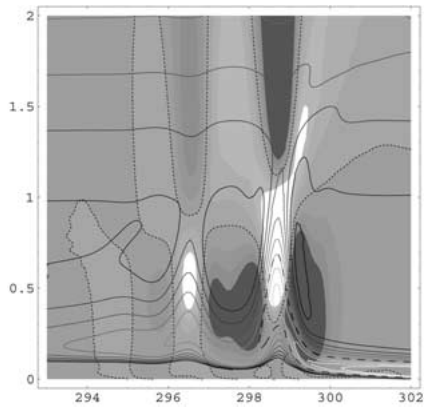
(d) Total vorticity Ω, represented as in Figure 4(a) and normal pressure gradient P_y represented by the shading separated by contours with values -0.0018 (darkest) to 0.0018 (lightest) in steps of 0.0006. The zero contour is dashed.
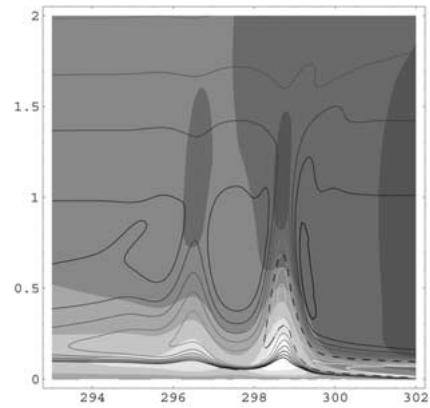
(e) Total vorticity Ω, represented as in Figure 4(a) and perturbation streamwise velocity u represented by the shading separated by contours with values -0.05 (darkest) to 0.15 (lightest) in steps of 0.05.

Figure 4. The subsequent development of the spike at $R = 10^5$. Figures 4(b–e) show the structures in Figure 4(a) in more detail.

(a) Total vorticity $\Omega(x, y)$ and vertical velocity v. Values of Ω are given by the contours in the range -0.4 (white) to 0.6 (black) in steps of 0.05 with the zero contour dashed. Values of v are represented by the shading separated by contours with values -0.1 (darkest) to 0.1 (lightest) in steps of 0.01. Again the zero contour is dashed.

(b) Wall vorticity (solid), wall pressure $100P(x, 0)$ (dotted) and pressure gradient $100P_x(x, 0)$ (dashed).

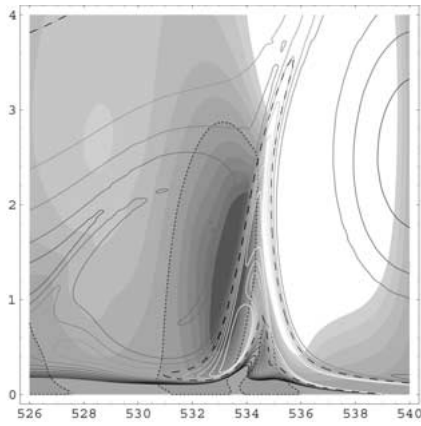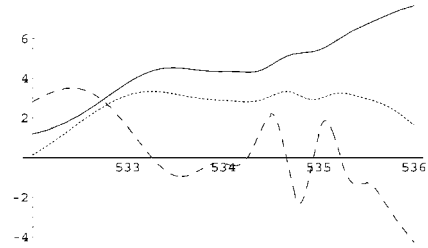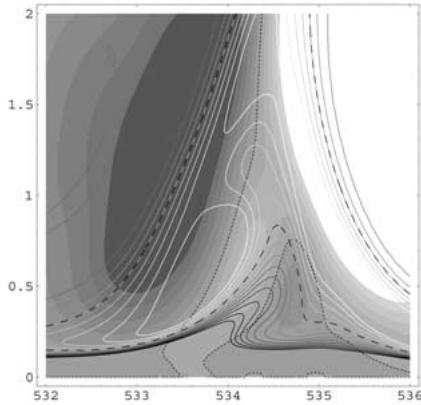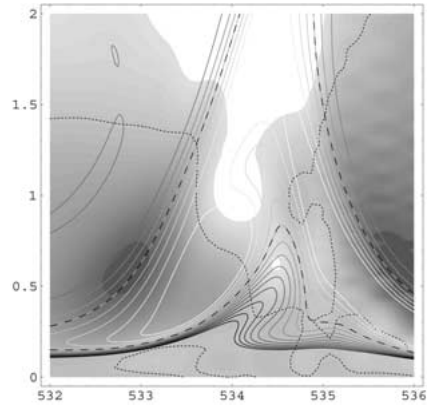(c) Total vorticity Ω and normal velocity v, represented as in Figure 5(a).

(d) Total vorticity Ω, represented as in Figure 5(a) and normal pressure gradient P_y represented by the shading separated by contours with values -0.03 (darkest) to 0.1 (lightest) in steps of 0.00133. The zero line is dashed.

Figure 5. Secondary eruptions at $R = 2500$. Figures 5(b–d) show the structures in 5(a) in more detail.

stream around $x = 535$. We see that the secondary vortex has grown significantly by this stage but also there is evidence of a secondary eruption of vorticity from close to the wall at $x = 534 - 5$, visible in Figure 5(a) and viewed in close up in Figures 5(b–d). The secondary eruption is slightly different from the first in that it is of increased vorticity, generated at the wall as a result of the large favourable pressure gradient erupting into the region of decreased vorticity being brought in from downstream. However, although of course at a smaller scale
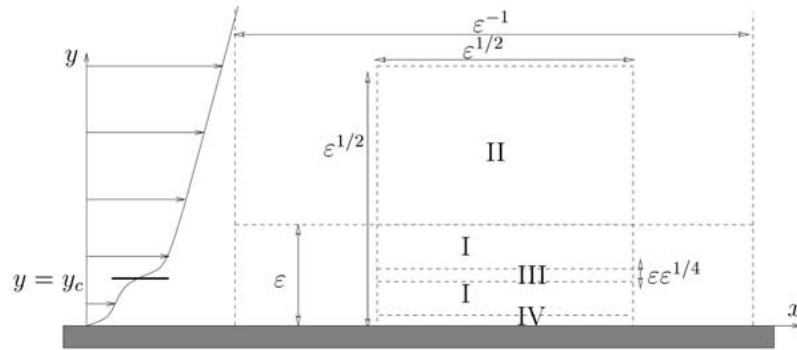
Figure 6. The disturbance structure close to the wall during spike formation as $R \to \infty$. Here $\epsilon = R^{-1/4}$ and the boundary layer is of thickness $O(1)$. The wall layer I is of thickness $O(\epsilon)$ and length $O(\epsilon^{-1})$, the length scale of the TS wave (which travels with speed $O(\epsilon)$) before spiking. This basic structure breaks down to shorter scaled disturbances of length $O(\epsilon^{1/2})$ which decay over a normal scale, II, also of $O(\epsilon^{1/2})$. The dynamics of the critical layer, III, situated at the velocity profile's inflection point is important in the formation of the secondary vortices but the viscous wall layer, IV, is essentially passive, at least in the initial stages. See [9].

than the first, it is broadly similar as may be seen in the pattern of localised regions of increased magnitude of v and P_y values. It is driven by the significant adverse pressure gradient now present on the downstream edge of the secondary vortex. It seems clear that this secondary eruption is responsible for the wavepacket-like signal in the wall pressure gradient at this station and that a similar, although incipient, eruption is the cause of the similar signal in Figure 4(b) at $x = 298 \cdot 5$.

The simulation continued to run for times significantly later than that considered in Figure 5 and there were several repeated secondary eruptions separated by intervals in which the basic structure was reestablished. The details of this late stage of the flow development is not considered in this paper but we did look at simulations with increased numerical resolutions which reproduced these secondary eruptions both in magnitude and broadly in phase and we feel that this is strong evidence of the accuracy and power of the numerical approach used. Recall that we are accurately tracing the development of a short-scaled flow close to the wall which develops in a wavetrain of TS waves which is of the order of 200 times as long.

4. The theoretical description of vortex generation and comparisons with the simulations

At medium-to-large Reynolds numbers the TS waves, which have wavelengths larger than the boundary-layer thickness, are well described, in both the two and three-dimensional cases, by the unsteady triple-deck equations or interactive-boundary-layer (IBL) equations ([29] and so on). These are a nonlinear set of equations derived from the Navier-Stokes equations and capture the interplay between the action of viscosity and inertia near the wall, where the flow is governed by the boundary-layer equations but with an unknown pressure, $\tilde{P}$, produced by the reaction of the inviscid flow just outside the boundary-layer to the small normal displacement velocities at the boundary-layer edge and caused by the waves. The wall-normal momentum equation reduces to the statement that, in the basic TS wave, normal pressure gradients inside the boundary layer are of secondary importance compared to streamwise gradients, at least until spiking occurs. Close to the wall, writing $y = \epsilon Y$, $x = \epsilon^{-1} X$, $t = \epsilon^{-2} T$ with $\epsilon = R^{-1/4}$

the governing equations for $[u, v] = [\epsilon \tilde{U}, \epsilon^3 \tilde{V}]$ and $P = \text{const} + \epsilon^2 \tilde{P}(X)$ are, in normalised terms,

$$\tilde{U}_T + \tilde{U}\tilde{U}_X + \tilde{V}\tilde{U}_Y = -\tilde{P}_X + \tilde{U}_{YY}, \tag{8}$$

$$\tilde{U}_X + \tilde{V}_Y = 0, \tag{9}$$

$$\tilde{U} - Y \to A, \quad Y \to \infty, \tag{10}$$

$$\tilde{P} = \frac{1}{\pi} \int_{-\infty}^{\infty} \frac{A_S}{X - S} dS, \tag{11}$$

where $-A$ is a measure of the increase in boundary-layer thickness. The vertical velocities at the edge of the boundary layer are $-\epsilon^2 A_X$, having grown from their smaller values close to the wall, and it is the action of wall-normal pressure gradients *outside* the boundary layer where $y = O(\epsilon^{-1})$ in reducing these to zero that generates the pressure P defined by (11).

Although the situation is clearly complicated by the finite Reynolds number and the large wave amplitude it is clear from Figures 2(a) and 2(b) that the disturbances are approximately governed by these equations in the sense that they capture the relevant physics and broad structural features. In particular, the values of the vertical velocity grow towards the boundary-layer edge before being reduced by the normal pressure gradients active outside the boundary layer where they are comparable in magnitude with the streamwise gradients. Within the boundary layer values of P_y are significantly smaller. Finally the behaviour of the vorticity contours across the bulk of the boundary layer suggests that this is being lifted as a whole in response to the flow in the wall layer, a lifting which is another theoretical prediction at high values of R. As mentioned in Section 3 the pattern in the contours of P_y is consistent with being caused by the streamline curvature due to this lifting.

The nonlinear inertial terms in (8) suggest that a wavebreaking singularity is possible, as in the shallow water equations for example, [30]. From the theoretical viewpoint, it is this singularity that governs the initial stages of the spike development after the initial growth of the TS wave, the flow separation and the strongly nonlinear development of the streamwise velocity profile away from its initial uniform shear $\tilde{U} = Y$ which are all governed by (8–11). The shortening streamwise lengthscales associated with such a singularity would provoke increasing values of wall-normal velocity, as seen in the computations. However, the large values of $\tilde{P}$ then generated through (11) would at first sight disallow the singularity structure. This was considered in [7] using the expansion

$$X - X_0 = c(T - T_0) + (T_0 - T)^{3/2}\xi, \tag{12}$$

$$\begin{aligned}[\tilde{U}, (T_0 - T)\tilde{V}] = \; &[\bar{U}(Y), 0] + (T_0 - T)^{1/2}[\tilde{U}_1(\xi, Y), \tilde{V}_1(\xi, Y)]+ \\ &(T_0 - T)[\tilde{U}_2(\xi, Y), \tilde{V}_2(\xi, Y)] \cdots , \end{aligned} \tag{13}$$

$$\tilde{P} = \tilde{P}_0 + (T_0 - T)^{1/2}\tilde{P}_1(\xi) + (T_0 - T)\tilde{P}_2(\xi) + \cdots \tag{14}$$

in (8–11) as $T \to T_0$ the time of the singularity, occuring at streamwise station X_0. Here $\bar{U}$ is the local velocity profile at wave-breaking and has an inflection point at $Y = Y_c$ say $(\bar{U}''(Y_c) = 0, \bar{U}(Y_c) = c)$. The pressure is found to satisfy

$$-a_1(\tilde{P}_1 - 3\xi \tilde{P}_1')/2 + a_2 \tilde{P}_1 \tilde{P}_1' = \mu \tilde{J}' \tag{15}$$

for a constant μ, which depends on the profile $\bar{U}$, and where $a_{1,2}$ are integral properties of $\bar{U}$. In the derivation of (15) some care must be taken over the flow in the critical layer (III), centred about $Y = Y_c$. This gives rise to the term $\tilde{J}(\xi)$ which represents a jump in scaled streamwise velocity across the layer. We consider this in more detail below, but, at these initial stages of the spike generation, the critical layer dynamics have no influence on the pressure development and in fact $\tilde{J}'$ is identically zero. The pressure is then determined by left-hand side of (15) which is a well-known similarity form describing wave breaking. The vertical velocity, increasing like $(T_0 - T)^{-1/2}$, is given by

$$\tilde{V}_1 = -\tilde{P}_1'(\bar{U} - c) \int_0^Y \frac{dv}{(\bar{U}(v) - c)^2}. \tag{16}$$

so that if $\bar{U}$ satisfies the finite-part integral condition

$$\int_0^\infty \frac{dY}{(\bar{U} - c)^2} = 0, \tag{17}$$

the vertical velocity, although not zero at the edge of the sublayer, at least does not grow to attain the larger values at the edge of the boundary layer that generate the displacement pressure and the singularity structure remains intact. The increasing pressure gradient does have an influence at the wall in region IV, effectively a Stokes layer of thickness $Y = O(T_0 - T)^{3/4}$, where a large wall vorticity ($\tilde{U}_Y = O(T_0 - T)^{-1/4}$) is generated due to viscous action although, due to the still relatively small velocity perturbations, the dynamics is linear. The large wall vorticity is seen in the computations as the first signal of spike formation. See Figure 2(c).

It is difficult in practice to test the value of the finite-part integral in (17) from data obtained from a numerical simulation or indeed from experiment (although see [8]) since to do so requires an accurate knowledge of the higher derivatives of the velocity profile. However we are able to look at the position of the inflection points that occur around $x = 315$ in the simulation with $R = 2500$ (illustrated in Figure 2) and identify which is likely to be active in the sense described above. Figure 7 shows the position of the inflection points present in the flow at the initial stages of the spike development. A shear minimum and maximum are visible downstream of $x = 308$. The minimum can be traced down towards the wall to the reduced values of vorticity generated in the separated region further downstream. The maximum moves outward. A second shear maximum/minimum is visible downstream of $x = 314$ at $y = 0.6$ approximately. The minimum rapidly moves outward with x and combines with the maximum described above. The lower maximum remains. It passes through the region of increased v values close to $x = 315$, $y = 0.6$ suggesting that it is this inflection point that is the relevant one in the theory, entering into Equation (17) through the value of c and in the vicinity of which Equation (15) may be expected to hold.

The theory captures well the initial stages of spike development, illustrated in Figure 2, when wall-normal pressure gradients are small within the boundary layer. As the length scales continue to shorten, due to the wave breaking influence described earlier and seen in Figure 2(c), new physics enters and, as in a nonlinear bore in shallow water, wave dispersion may be expected to act to radiate the energy of wavebreaking into a wavetrain (see [31] in a simple situation). This causes the appearance of the pressure maximum seen in Figure 3(b). The details of the theory which describes this stage of development are presented in [9] and
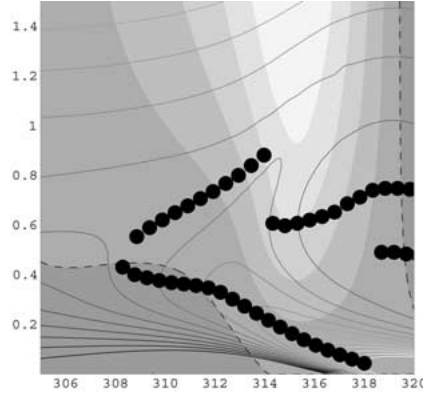
Figure 7. The vorticity and vertical velocity visualised as in Figure 2(a) with the position of inflection points in the velocity profile indicated by a lines of filled circles.

summarised below. The governing equation for this process inside the boundary layer is the Benjamin-Ono equation and it arises due to the action of normal pressure gradients. The vertical velocity at the edge of region I, predicted by (16–17) is reduced to zero by normal pressure gradients in a square region (II) extending just outside the viscous sublayer but buried within the vertical scale of the boundary layer; see Figure 6. Here $\bar{U}$ is well approximated by a profile with a scaled constant shear (equal to λ say) and v satisfies Laplace's equation. Note that this decay takes place *within* the scale of the boundary-layer and this region is distinct from the region outside the boundary layer where the displacement velocity caused by the wave itself decays. Over these scales normal pressure gradients are generated and their streamwise variation gives rise to streamwise velocity gradients which, as the singularity develops, strengthen and eventually enter the inertial balance (15). This fixes the shortened streamwise lengthscale illustrated in Figure 6 and occurs when $(T_0 - T) = O(\epsilon)$. This implies a new expansion with $t = t_0 + \epsilon^{-1}\tilde{t}$, $x = x_0 + c\tilde{t} + \epsilon^{1/2}\tilde{x}$ for constants t_0 and x_0, and

$$[\epsilon^{-1}u, \epsilon^{-3/2}v] = [\bar{U}(Y), 0] + \epsilon^{1/2}[\tilde{u}_1(\tilde{x}, Y, \tilde{t}), \tilde{v}_1(\tilde{x}, Y, \tilde{t})] + \epsilon[\tilde{u}_2(\tilde{x}, Y, \tilde{t}), \tilde{v}_2(\tilde{x}, Y, \tilde{t})] + \cdots,$$
(18)

$$\epsilon^{-2}P = \tilde{p}_0 + \epsilon^{1/2}\tilde{p}_1(\tilde{x}, \tilde{t}) + \epsilon\tilde{p}_2(\tilde{x}, \tilde{t}) + \cdots.$$
(19)

This is substituted in the full equations (1–2), again with $y = \epsilon Y$ to obtain, similarly to (15),

$$a_1\tilde{p}_{1\tilde{t}} + a_2\tilde{p}_1\tilde{p}_{1\tilde{x}} = \frac{1}{\pi}\int_{-\infty}^{\infty}\frac{\tilde{p}_{1ss}\mathrm{d}s}{\tilde{x} - s} + \mu\tilde{J}_{\tilde{x}},$$
(20)

with again $\mu\tilde{J}_{\tilde{x}}$ a contribution from the critical layer. This is to be solved with initial and boundary conditions consistent with the solution of (15), which governs the flow at earlier times and over longer scales where the influence wall-normal pressure gradients is less important. A solution to this system, with these conditions is given in Figure 8. Its similarity to the wall-pressure distribution in Figures 3(b) and 4(b) is striking, taking into account the influence of the secondary eruptions. This calculation is for $\mu = 0$ but the distribution is similar if $\mu/a_1 < 0$. If $\mu/a_1 > 0$, by contrast, then the system is ill-posed and a wave packet of small-scale oscillations is seen, a point we return to below. The Korteweg-de Vries equation which governs the shallow-water bore may be obtained in this context for the special case of
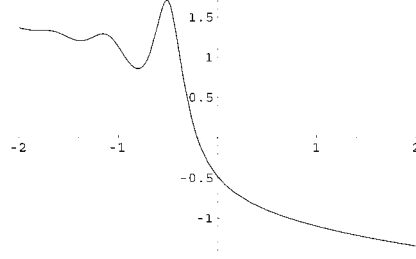
Figure 8. The theoretical prediction for the streamwise pressure distribution obtained through a solution of (9) and (10) with $\mu = 0$ and suitable initial conditions. See [9]. Compare with the distributions in the simulations in Figures 3(b) and 4(b).

symmetric disturbances in a channel. In this case the normal pressure gradient is generated by a streamline curvature effect and gives rise to a term proportional to $\tilde{p}_{1\tilde{x}\tilde{x}\tilde{x}}$ on the right hand side of (20). This mechanism is also present across region I in the boundary-layer case and is visible in the triangular structures in Figure 3(d). Its influence is theoretically less important than the mechanism described above, being asymptotically smaller as $R \rightarrow \infty$ although is not clear which is in fact dominant at the Reynolds numbers considered in the simulations.

The calculation of $\tilde{J}$ proceeds as follows. The critical layer has thickness $O(\epsilon^{5/4})$ and we write $y = \epsilon Y_c + \epsilon^{5/4}\zeta$, with ζ of order one. If $\bar{U} \sim c + b_1(Y - Y_c) + b_3(Y - Y_c)^3 + b_4(Y - Y_c)^4 + \cdots$ with b_n constants, then we obtain

$$[\epsilon^{-1}u, \epsilon^{-3/2}v] = [c + \epsilon^{1/4}b_1\zeta, -\epsilon^{1/2}b_1^{-1}\tilde{p}_{1\tilde{x}}] \tag{21}$$

from the limit of the solution in I as $Y \rightarrow Y_c$. Expanding the local shear, which dominates the vorticity, as

$$u_y = b_1 + \epsilon^{1/2}(3b_3\zeta^2 + 6b_1^{-2}b_3\tilde{p}_1) + \epsilon^{3/4}(4b_4\zeta^3 + a_{13}\tilde{p}_1 + \tau(\tilde{x}, \zeta)) \tag{22}$$

where a_{13} is a constant depending on integral properties of the profile $\bar{U}$, and substituting into the vorticity equation (3) gives

$$b_1\zeta\tau_{\tilde{x}} - b_1^{-1}\tilde{p}_{1\tilde{x}}\tau_\zeta = -6b_1^{-3}(b_1b_3\tilde{p}_{1\tilde{t}} - 2b_4\tilde{p}_1\tilde{p}_{1\tilde{x}}). \tag{23}$$

Now

$$\tilde{J} = b_1^{-1}\int_{-\infty}^{\infty}\tau\,\mathrm{d}\zeta. \tag{24}$$

and it may be shown (see [32]) that

$$\mu\tilde{J}_{\tilde{x}} = 6b_3b_1^{-4}\tilde{p}_{1\tilde{x}}\int_{-\infty}^{\infty}\frac{(\tilde{p}_{1\tilde{t}}(s,\tilde{t}) + a_1^{-1}a_2\tilde{p}_1\tilde{p}_{1s}(s,\tilde{t}))\mathrm{d}s}{\tilde{p}_1(\tilde{x},\tilde{t}) - \tilde{p}_1(s,\tilde{t})}. \tag{25}$$

Here we have used the additional result that when (17) is first satisfied in the flow $a_1/a_2 = -b_1b_3/2b_4$. See [9].

As the dispersive effects first enter, the contribution to the momentum balance from the dynamics in the critical layer begins to have an influence. However it has little qualitative effect on the flow solution until regions are generated where $\tilde{p}_{1\tilde{x}}$ is small, which subsequently give rise to the pressure max/min being generated. From (21) the vertical velocity at the critical level is $-b_1^{-1}\tilde{p}_{1\tilde{x}}$ to first order and the generation of a pressure max/min leads to an alteration
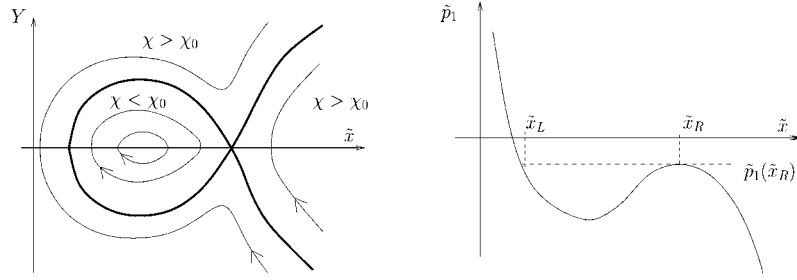
Figure 9. The flow at the critical level. The vortex is contained in the interval $\tilde{x}_L < \tilde{x} < \tilde{x}_R$ with $\chi = \chi_0$ representing the separating streamline.

of sign in the vertical velocity with $\tilde{x}$ and hence to regions of recirculating flow or a rolling-up spanwise vortex in a frame traveling with speed ϵc. The initial stages of this process are described in [9, 12] who show it to be governed by a strong interaction between the effects of normal pressure gradients and the critical layer jump term, $\tilde{J}_{\tilde{x}}$, leading to an explosive growth in the size and length of the vortex. If μ, proportional to b_3, is relatively small, in contrast, corresponding to a relatively broad shear layer, [9, 10] show that the interaction may be delayed until after the vortex has been formed. It is of interest to note that b_3 is identically zero as an inflection point pair is generated and that Figure 7 suggests that the spiking takes place just downstream of such a generation. As a result, this special limiting case may be relevant in these simulations. In this situation τ satisfies

$$\tau_{\bar{t}} + b_1 \zeta \tau_{\tilde{x}} - b_1^{-1} \tilde{p}_{\tilde{x}} \tau_\zeta = 0, \tag{26}$$

with $\bar{t}$ now denoting the relatively fast timescale (faster by a factor $\epsilon^{-1/4}$ than that over which $\tilde{p}_1$ develops) over which fluid particles enter and leave the critical level or, if captured and on a closed orbit, recirculate within it. At high Reynolds numbers, viscosity does not have time to act and (26) merely expresses the conservation of vorticity for any fluid particle in this locally two-dimensional flow. The effects of $\tilde{J}$ on the subsequent flow development are detailed in [10] where it is shown that it may give rise to a relative lengthening of the vortices. Here we note that the paths followed by the particles satisfy $d\tilde{x}/d\bar{t} = b_1 \zeta$, $d\zeta/dt = -b_1^{-1} \tilde{p}_{1\tilde{x}}$, *i.e.*, $d^2\tilde{x}/d\bar{t}^2 = -\tilde{p}_{1\tilde{x}}$ which gives rise to closed trajectories upon which the vorticity is constant. The vorticity is a function of $\chi = b_1 \zeta^2/2 + b_1^{-1} \tilde{p}_1$ as seen in Figure 9.

Further comparison with the simulations suggests that there is in fact considerable diffusion of the vorticity between closed streamlines in the simulations; indeed different critical-layer dynamics may be active at the present computational Reynolds numbers. One possible situation is suggested in [33] which considers velocity profiles with the integral of (17) being of $O(\epsilon^{1/2})$ instead of zero. The profile is then marginally unstable to a range of relatively long Rayleigh waves which grow on a timescale similar to that of the $O(\epsilon^{1/2})$-sized disturbances to the TS pressure profile considered in (19). For smaller $O(\epsilon)$ amplitude disturbances, the non-linear streamwise inertial effects are reduced so that the pressure equation (20) is linearised. The critical-layer dynamics remain nonlinear but the layer is thinner and as a consequence becomes unsteady and viscous and of a type studied by [34], for example which examines the nonlinear development of a single wave mode. In the present context however all wave modes are active and interact through the critical-layer-jump term in (20). The large-time solutions are similar to those studied by [34] with the jump governed by a balance of unsteady and viscous dynamics inside the critical layer and the initial exponential growth reduced to slower

algebraic growth through viscous saturation. The large-time wave form is not sinusoidal but depends on the flow parameters. Certain solutions exhibit relatively long vortices separated by short-scaled peaks in the pressure, very similar to the flow pattern seen in Figures 4(c–e).

We now consider the secondary eruptions illustrated in the simulations of Figure 5. The theory here considers pressure gradients of a magnitude such that the wall layer (IV) is linear. As amplitudes increase or scales shorten, as a result of the generation of vortices discussed above, the full inertial terms become active. Although the theoretical details are not yet clear and are the subject of current investigation, it seems likely that the process described earlier in this section may be repeated but on a shorter scale as part of a cascade. One point of interest is that, as noted in the discussion of Figure 7, the inflection point of relevance in these secondary eruptions is a vorticity minimum. This corresponds to a change in sign in b_3 and hence μ for which the theory predicts a wave-packet of rapidly growing, small-scale pressure oscillations which may explain the oscillations seen in Figures 4(b) and 5(b).

5. Discussion

As mentioned in Section 1 the above theory is expected to be of relevance to unsteady separation as well as transition. Indeed Figures 3(a) and 4(a) suggest that the large amplitude TS disturbances we consider could be viewed as a series of developing vortices travelling downstream through a flat plate boundary layer. The spiking behaviour and its description and explanation may then be considered in the context of secondary separation and secondary-vortex generation. Computations of such processes forced by a single fully-developed stationary vortex exterior to a boundary layer have been carried out by [14, 15]. The flow structures they find are very similar to those here and suggest that similar detailed comparisons with the present theory could be made and that the processes described in this paper are similar to the so-called large-scale interaction described by [15]. There are intriguing differences nonetheless: first, the processes that would appear to correspond to our secondary eruptions occur before those corresponding to our secondary vortex generation; second, this short-scaled development arises in a region of reversed flow in their context. These two features may be connected in that the second, taken together with the property that the exterior vortex is stationary, suggests that the value of c in (17) is small. The developing disturbance is then hardly advected downstream and a stronger interaction with the wall layer (IV) is to be expected, perhaps occurring before the incursion of the dispersive terms which we have shown to be responsible for the generation of secondary vortices. This observation might well explain the first feature, making a study of small c values worthwhile.

The approach described in Section 4 has been successful in clarifying the complicated mechanisms and structures at work in the two-dimensional simulations of Section 3 and in identifying the physical approaches behind them. In addition the extensions and limiting cases mentioned which build upon this basic approach promise to shed more light upon the process, and we have claimed that these structures are related to those seen in computations of unsteady planar separation and caused by similar mechanisms. There is somewhat less detailed agreement with experimental and simulated studies of TS wave transition because of the strongly three-dimensional nature of the late stages of that process. There are broad similarities between the two- and three-dimensional cases however. These include the obvious importance of critical layer dynamics and vertical velocity distributions in vortex formation and, more fundamentally, the associated reduction in length-scale. The theory identifies a mechanism,

clearly active in two dimensions, through which normal pressure gradients, which enter as the scales shorten, can act to generate pressure maxima and minima which directly induce the vortices. These similarities indicate that an extension of the theory to cover three-dimensional influences is worth pursuing. Such an extension is at present underway by Mr. J. Marshall at University College London who is investigating the effect of a spanwise pressure gradient in generating a significant spanwise velocity w of size $O(\epsilon^{13/8})$ in the critical layer over a spanwise lengthscale $O(\epsilon^{9/8})$, measured by $\tilde{z}$. This can act to intensify the vorticity through the vortex-stretching mechanism. In essence the vorticity at the critical level, $\tau(\tilde{x}, \zeta, \tilde{z})$, is governed by the pair of equations

$$b_1 \zeta w_{\tilde{x}} - b_1^{-1} \tilde{p}_{1\tilde{x}} w_\zeta = -\tilde{p}_{\tilde{z}}, \tag{27}$$

$$b_1 \zeta \tau_{\tilde{x}} - b_1^{-1} \tilde{p}_{1\tilde{x}} \tau_\zeta = w_{\tilde{z}} - 6b_1^{-3}(b_1 b_3 \tilde{p}_{1\tilde{t}} - 2b_4 \tilde{p}_1 \tilde{p}_{1\tilde{x}}). \tag{28}$$

As before, the jump $\tilde{J}(\tilde{x}, \tilde{z}, \tilde{t})$ is obtained by integrating τ in ζ and interacts with $\tilde{p}_1$ through (20). One important result from this work indicates that, even for initially mild spanwise variations, as the pressure max/min is generated the three-dimensional influences on the critical-layer jump dominate over the two-dimensional influences described in this paper.

References

1. N.D. Sandham and L. Kleiser, The late stages of transition to turbulence in channel flow. *J. Fluid Mech.* 245 (1992) 319–348.
2. Y.S. Kachanov, Physical mechanisms of laminar-boundary-layer transition. *Annu. Rev. Fluid Mech.* 26 (1994) 411–482.
3. S. Bake, H.H. Fernholz and Y.S. Kachanov, Resemblance of K- and N- regimes of boundary-layer transition at late stages. *Eur. J. Mech., B Fluids* 19 (2000) 1–22.
4. G. Han, A. Tumin and I. Wygnanski, Laminar-turbulent transition in Poiseuille pipe flow subjected to periodic perturbation emanating from the wall. Part 2, Late stage of transition. *J. Fluid Mech.* 419 (1999) 1–27.
5. U. Rist and H. Fasel, Direct numerical simulation of controlled transition in a flat-plate boundary layer. *J. Fluid Mech.* 298 (1995) 211–248.
6. C.R. Smith, J.D.A. Walker, A.H. Haidari and U. Soburn, On the dynamics of near-wall turbulence. *Phil. Trans. R. Soc. London* A336 (1991) 131–175.
7. F.T. Smith, Finite time break-up can occur in any unsteady interacting boundary layer. *Mathematika* 35 (1988) 256–273.
8. F.T. Smith and R.I. Bowles, Transition theory and experimental comparisons on (a) amplification into streets and (b) a strongly nonlinear break-up criterion. *Proc. R. Soc. London* A439 (1992) 163–175.
9. L. Li, J.D.A. Walker, R.I. Bowles and F.T. Smith, F.T., Short-scale breakup in unsteady interactive layers: local development of normal pressure gradients and vortex wind-up. *J. Fluid Mech.* 374 (1998) 335–378.
10. R.I. Bowles, On vortex interaction in the latter stages of boundary-layer transition. In: F. Hasel and H. Saric (eds.), *Laminar-Turbulent Transition (IUTAM Symposium, Sedona, Arizona, USA, 1999*, Berlin: Springer-Verlag (2000) pp. 275–280.
11. R.I. Bowles, Transition to turbulent flow in aerodynamics. *Phil. Trans. R. Soc. London* A358 (2000) 245–260.
12. F.T. Smith, R.I. Bowles and J.D.A. Walker, Wind-up of a spanwise vortex in deepening transition and stall. *Theor. Comp. Fluid Dyn.* 14 (2000) 135–165.
13. M. Nishioka, N. Asai and S. Iida, An experimental investigation of the secondary instability. In: R. Eppler and H. Fasel (eds.), *Laminar-Turbulent Transition (IUTAM Symposium, 1979, Stuttgart)*. Berlin: Springer-Verlag (1979) pp. 37–46.
14. K.W. Brinckmann and J.D.A. Walker, Instability in a viscous flow driven by streamwise vortices. *J. Fluid Mech.* 432 (1995) 127–166.

15. A.V. Obabko and K.W. Cassel, Large-Scale and Small-Scale Interaction in Unsteady Separation, 2000, AIAA Paper 2000-2469, Fluids 2000, Denver, Colorado, June 19-22.
16. C. Davies and P.W. Carpenter, Numerical simulation of the evolution of Tollmien-Schlichting waves over finite compliant panels. *J. Fluid Mech.* 335 361–392.
17. C. Davies and P.W. Carpenter, A novel velocity-vorticity formulation of the Navier-Stokes equations. Pt. 2: Global behaviour corresponding to the absolute instability of the rotating-disk boundary layer. *University of Warwick, Fluid Dynamics Research Centre, Tech. Rept* 2000/1.
18. C. Davies and P.W. Carpenter, A novel velocity-vorticity formulation of the Navier-Stokes equations with applications to boundary layer disturbance evolution. *J. Comp. Phys.* 172 (2001) 119–165.
19. C. Davies and P.W.Carpenter, Global behaviour corresponding to the absolute instability of the rotating-disk boundary layer. *J. Fluid Mech* (2000) submitted.
20. C. Davies, Disturbance development in Blasius flow over a compliant panel. In: *3rd European Fluid Mechanics Conference*, Göttingen, Germany (1997)
21. P.W. Carpenter, C. Davies and D.A. Lockerby, A novel velocity-vorticity method for simulating the effects of MEMS actuators on boundary layers. *Proc. 3rd Asian CFD Conf., Bangalore, India, Indian Inst. Bangalore* (2000) pp. 44–49.
22. P.W. Carpenter, D.A. Lockerby and C. Davies, Numerical simulation of the interaction of MEMS actuators and boundary layers. *AIAA Journal* 40 (2002) 67–73.
23. P.W. Carpenter, A.D. Lucey and C. Davies, Progress on the use of compliant walls for laminar-flow control. *J. Aircraft* 38 (2001) 504–512.
24. C. Davies, P.W. Carpenter and D.A. Lockerby, A novel velocity-vorticity method for simulating boundary-layer disturbance evolution and control. In: H. Fasel and W.S. Saric (eds.), *Laminar-Turbulent Transition (IUTAM Symposium, Sedona, Arizona, USA, 1999)*. Berlin: Springer-Verlag (2000) pp. 313–318.
25. S. Houten, J.J. Healey and C. Davies, Nonlinear evolution of Tollmien-Schlichting waves at finite Reynolds numbers. In: H. Fasel and W.S. Saric (eds.), *Laminar-Turbulent Transition (IUTAM Symposium, Sedona, Arizona, USA, 1999.* Berlin: Springer-Verlag (2000) pp. 181–186.
26. S. Houten, J.J. Healey and C. Davies, Direct numerical simulation of wave-envelope steepening effects in the Blasius boundary layer. (2000) in preparation.
27. H.L. Meitz and H.F. Fasel, A compact-finite difference scheme for the Navier-Stokes equations in vorticity-velocity formulation. *J. Comp. Phys* 157 (2000) 371–403.
28. F.T. Smith and O.R. Burggraff, On the development of large-sized short-scaled disturbances in boundary layers. *Proc. R. Soc. London* A399 (1995) 24–55.
29. F.T. Smith, On the nonparallel stability of the Blasius boundary layer. *Proc. R. Soc. London* 366 (1979) 91–109.
30. G.B. Whitham, *Linear and Nonlinear Waves.* New York: Wiley-Interscience (1974) 791 pp.
31. H. Peregrine, Calculations of the development of an undular bore. *J. Fluid Mech.* 25 (1966) 321–330.
32. F.T. Smith and R.J. Bodonyi, Properties of a time-dependent nonlinear viscous critical layer. *Stud. Appl. Maths.* 77 (1987) 129–150.
33. R.I. Bowles, Nonlinear instability of the shear layer in end-stage transition. (2002) in preparation.
34. M.E. Goldstein and L.S. Hultgren, Nonlinear spatial evolution of an externally excited instability wave in a free shear layer. *J. Fluid Mech.* 197 (1988) 295–330.